JOURNAL OF PROPULSION AND POWER
Vol. 24, No. 2, March–April 2008

Analysis of Injecting Wall Inclination on Segmented Solid Rocket Motor Instability

Chi Cong Nguyen,* Frédéric Plourde,† and Son Kim Doan‡
Laboratoire d'Études Thermiques/École Nationale Supérieure de Mécanique et d'Aérotechnique, 86961 Chasseneuil Futuroscope, France

DOI: 10.2514/1.29551

The influence of α solid propellant inclination angle was analyzed through small-scale setup simulations. Two injected blocks separated by thermal protection reproduced the main geometric solid rocket motor features, and a dual phenomenon driving interactions between the shear layer and injecting wall vortex-shedding phenomena was clearly identified at any inclination angle. A threshold angle level was also pinpointed, and it literally controls either the decrease of oscillation levels for small angles or the increase of the coupling energy involved. Under similar dynamic conditions, a decreasing factor of two was observed between $\alpha = 0$ and -1.5 deg, whereas an even higher amplification factor was noted for $\alpha = -2$ deg. Correlation coefficients and phase-averaged analysis have allowed the authors to clearly explain these opposed trends by depicting the wall and shear-layer interactions along the chamber.

Nomenclature

a	=	sound velocity, m/s
$f_n = na/2L$	=	nth longitudinal acoustic mode, Hz
H_c	=	channel height, m
H	=	nozzle height, m
$It = \sqrt{\overline{u'^2} + \overline{v'^2}}/aM$	=	turbulence intensity
L	=	channel length, m
L_v	=	distance between the obstacle and the nozzle location, m
$M = q_m/a\rho wH_c$	=	characteristic Mach number based on the mass flow rate
$M^* = M/(1 + L_v/H_c \tan\alpha)$	=	modified Mach number
P	=	static pressure, Pa
q_m	=	total mass flow rate, kg/s
$R_{x'y'} = \overline{x'(t)y'(t+\tau)}/\sqrt{\overline{x'^2(t)}}\sqrt{\overline{y'^2(t)}}$	=	correlation coefficient of arbitrary functions of time x' and y'
$S_{x'} = s_{x'}/\overline{x'^2}$	=	normalized power spectral density, Hz^{-1}
$s_{x'}$	=	power spectral density
T	=	period, s
$\bar{U} = \bar{u}/U_0$	=	normalized mean velocity in each section
U_0	=	characteristic velocity, m/s
$\bar{u}$	=	mean velocity in each section, m/s
u, v	=	velocity component in X and Y directions, m/s
w	=	channel width, m
X, Y	=	nondimensional axis normalized by H_c
α	=	angle of inclination
ρ	=	density, kg/m^3
τ	=	time delay, s
Ω_z	=	vorticity normalized by U_0/H_c

Superscripts

$'$	=	fluctuating component
$\bar{}$	=	time averaged
$\langle\rangle$	=	phase averaged

I. Introduction

ALTHOUGH solid rocket motor (SRM) design is of paramount importance in guaranteeing a perfect launcher mission, segmented motors present a substantial and well-documented risk of unstable behavior during firing. Titan IV and, more recently, P230 Ariane 5 boosters were found to be unstable, which entailed pressure fluctuations in the internal chamber signaling vibrations. The latter may vary in amplitude, but their transmission to the payload via the launcher structure remains possible. Although shock absorber systems can be introduced, vibrations directly interact with launcher efficiency through overloading. In conclusion, instability arises from the interaction of several factors; thorough understanding of these effects and their coupling could facilitate improved design of the next generations of internal chambers.

Studies of SRM instability are numerous in the literature; they include data and feedback experiments ranging from a subscale model to a real-scale launcher. From a more fundamental point of view, even though Culick [1] was the first to develop a mean flow solution for the internal flowfield of a circular propellant, simplified acoustic balance analysis was rapidly found to fail to predict instability in segmented motors [2]; unsteady mechanisms such as vortex shedding were simply not taken into account in the model's framework. Flandro [3] and, more recently, Flandro and Majdalani [4] went on to improve acoustic balance by introducing additional energy source/sink terms arising from rotational flow effects; according to the authors, these terms may enhance our understanding of instability. However, even if such tools are of particular help in SRM internal design, closer investigation of the internal flowfield is needed to ensure fuller depiction of complex phenomena. Meanwhile, in studies of instability from the standpoint of aerodynamics, numerical as well as cold gas simulations have been extensively used. It seems quite apparent that since the initial numerical simulations in descriptions of internal flowfield development were carried out, appreciable enhancement of computing power has given fresh impetus to our understanding of highly specific flows. To the authors' knowledge, Lupoglazoff and Vuillot [5] were the first researchers to numerically demonstrate the existence of wall vortex shedding, i.e., roll up resulting from interactions between the main flow and the flow from burnt gas due to

Received 1 January 2007; revision received 8 October 2007; accepted for publication 12 October 2007.

*Scientist, 1 Avenue Clément Ader, BP 40109.
†Senior Scientist, Centre National de la Recherche Scientifique, 1 Avenue Clément Ader, BP 40109.
‡Emeritus Professor, 1 Avenue Clément Ader, BP 40109.

propellant combustion. Unsteady flow evolution in a porous chamber with surface mass injection was investigated numerically with large-eddy simulation [6–8], and the authors accurately depicted the three successive regimes of flow development: laminar, transitional, and fully turbulent. When aerodynamic instability is highlighted, combustion is generally viewed in terms of inlet boundary conditions. Acoustic coupling is initiated with impingement of vortices upon the nozzle or other obstacles presenting acoustic feedback. A cold gas experimental setup has been developed so as to expressly analyze internal flowfield behavior and potential unstable mechanisms. Cold gas setup is generally based upon reproduction of characteristic nondimensional numbers, whereas propellant combustion is simulated by injecting air through porous walls. Such simulations are valid insofar as geometry variation time is considerably shorter than the actual characteristic time of flow transit in the chamber. In one example, simulation of the internal flowfield of Ariane 5 SRM was carried out by a Mach and Strouhal number similitude in the MICAT cold gas setup [9,10]. Cold gas setup was first used to characterize development of flowfield when induced by porous wall injection alone. The mean flowfield [11,12] and turbulence development [13,14] and the effects induced by the use of porous material [15] were investigated in several geometric conditions, i.e., using cylindrical or bidimensional chambers. Given the advancement of the studies and findings arising from cold gas setup, it has undeniably yielded concrete results of substantial interest to the scientific community. For instance, the analysis of mean and fluctuating velocities in a simulated cylindrical port rocket chamber performed by Dunlap and Brown [11] was of major importance and, to the authors' knowledge, they were the first scientists to have experimentally observed vorticity generation in the vicinity of injecting walls. Thereafter, cold gas setup was developed to assess Taylor flow instability [16] and, with the experimental results achieved, the theoretical work carried out by Griffond and Casalis [17] and Casalis et al. [18] was satisfactorily validated. Their findings focused mainly on the dynamic and geometric conditions that favor a vortex-shedding mechanism in an undisturbed geometric porous wall channel. To better depict unstable mechanisms, nonlinear analyses and computational studies on more idealized systems were also conducted [19,20]. For instance, Hegab and Kassoy [20] recently quantified the numerical wall vorticity dynamics caused by transient sidewalls.

Even if the geometry of a real propellant booster is not taken into full account, i.e., some cold gas setups are not cylindrical, the effect of propellant segmentation has indeed been studied (for instance, results attained from the MICAT setup facility close-up analysis of the effect of restrictors). Restrictors, also named inhibitors, induce shear in the main flow when located in such a way as to inhibit front-face combustion, and the process results in vortex-shedding mechanisms. Vetel et al. [9] have demonstrated that, under specific dynamic conditions, although the vortex shedding arising from these inhibitors or obstacles does not constitute the main source of instability, its presence triggers the development of a second vortex-shedding mechanism close to injecting walls. In other words, the presence of an unsteady mechanism in the main flow actually initiates the latter. Comparisons between results from small-scale solid propellant rocket motor and cold gas setups were recently published and provide solid confirmation of these findings [21]. Experiments carried out on the combustor included nonablative inhibitors on the final segment forward face; four inhibitor shapes were tested, each corresponding to specific pressure oscillation behavior. The cold gas setup was designed so as to replicate the general features of the internal geometry of this combustor at two different burning times and the pressure measurements were found to reproduce the acoustic response of firing tests with satisfactory agreement. We may conclude that the cold gas setup allows researchers to accurately describe the main oscillating mechanisms arising with regard to simulated burning time and obstacle shape. In addition to this, a convection velocity model has been proposed to explain how resonance frequency evolves during firing tests. Cold gas setups are resultantly of prime importance and may enhance our understanding of the most significant parameters driving instability in SRM. On another score, studies of the influence of the small tapered angle of the propellant blocks have recently been carried out. Modern SRMs incorporate this angle so as to reduce contact between casting mandrels and the propellant, thereby facilitating their removal. Sams et al. [22] recently studied the development of internal flowfield with tapered side walls, thereby underscoring such effects from an analytical standpoint. To our knowledge, Sams et al. [22,23] were the first to closely analyze tapered wall effects in a porous ducted channel devoid of restrictors. Their findings bolstered the hypothesis that tapered segments significantly influence pressure and velocity profiles and, most importantly, shed light on generation close to the walls.

In this paper, the authors are pursuing a similar objective but with more complex geometry, i.e., analyzing the effect of tapered walls in segmented solid rocket motors. To do so, we have carried out cold gas simulations and, for that reason, the MICAT experimental setup was modified to analyze the α-angle tapered wall influence. To the authors' knowledge, most previous cold gas setups were not equipped with tapered sidewalls ($\alpha = 0$ deg); what is more, the scale model we have used was designed to reproduce an internal flowfield of segmented SRM. Thanks to the analysis of available data achieved with the MICAT experimental setup [9,10,12], the different unsteady vortex-shedding mechanisms are seen to arise in the last propellant segment. In accordance with these results, only the last injecting block was equipped with various α-angle tapered conditions.

Our paper is organized as follows. First, the cold gas experimental setup and its modifications during equipment of the last injecting block are detailed, along with the experimental dynamic conditions. Second, main flow features such as velocity profiles, vorticity, and pressure fluctuations are described for both nontapered side walls ($\alpha = 0$) and several α angles. Last, and from these data, the role of α in the two vortex-shedding mechanisms and their interactions is explained and, more generally speaking, the effect of α on coupling is brought into focus.

II. Experimental Setup and Measurement Systems

All the results presented hereinafter were obtained experimentally and the experiments were conducted on the MICAT cold gas experimental setup, which was initially developed to analyze instability arising in large, segmented SRM. The model ($L = 0.623$ m) was built to reproduce the main geometric and dynamic characteristics of Ariane 5 segmented motors, i.e., segmented blocks and a submerged nozzle. It was bidimensional, designed to facilitate experimental investigations: as shown in Fig. 1, two injecting blocks are located in the chamber separated by an embedded obstacle. As mentioned in the Introduction, combustion is simulated by injecting air at an ambient temperature through a porous plate made of 2-μm-diam, sintered-bronze spheres; mass flow rate uniformity is controlled by a feeding system composed of several sonic inlet injectors, honeycomb and isolated cells that feed a specific porous wall surface. The porosity and thickness of the porous plate allows for isolation of injecting noise from pressure signals generated by the flow to be studied. Each of these injecting blocks was manufactured with α characteristic tapered injecting sidewall angles ($\alpha = 0, -0.5, -1.0, -1.5$, and -2.0 deg), and the porous wall was

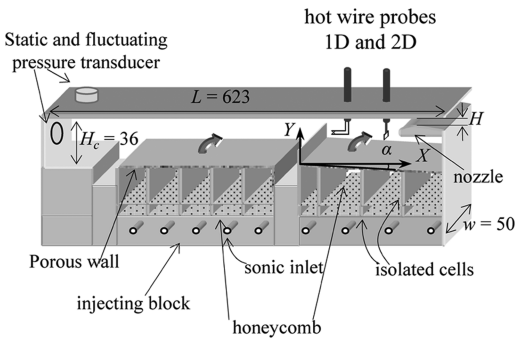

Fig. 1 Experimental setup.

flush-mounted to the injecting blocks. A submerged nozzle was located at the rear part of the chamber to ensure the acoustic isolation of the chamber from the outer environment; the height of the nozzle throat could be varied, thereby controlling the characteristic Mach number M.

The mean and fluctuating pressure signals were measured at the head end by a flush-mounted piezoelectric quartz transducer with an accuracy rate of 10 and 0.02 Pa for static and fluctuating pressure, respectively. The velocity signals were recorded from a 5 μm single miniature probe for spectral analyses and from a 5 μm X miniature probe for mean characterization; estimation of errors for the mean and fluctuating data was found to be equal to ± 1 and $\pm 2.5\%$, respectively, whereas mass flow rate measurement accuracy was $\pm 2\%$. Pressure and velocity signals were recorded by a 12-bit A/D board, and sampling frequency was set equal to 10 kHz, whereas maximum spectral frequency was found to be less than 1000 Hz. A fast Fourier transform (FFT) algorithm was used to estimate spectral answers constructed by an average of 50 blocks of 4096 points with a resolution frequency of 2.44 Hz. To assess correlation coefficients between fluctuating signals, finite inverse Fourier transform was used. Phase-averaged quantities were obtained by averaging the instantaneous velocities in one single period corresponding to the main excited frequency found in the spectral distribution. The period was subdivided into 80 time intervals and phase-averaged data were processed with 2500 cycles. Because considerable effort went into ensuring the accuracy of the data, the phase-averaged focus facilitates qualitative insights into the vortex-shedding mechanisms.

III. Tapered Sidewall Influence on Internal Flowfield

A. Average and Fluctuating Fields

The first step in depiction of the α tapered sidewall effect is to study flowfield behavior with regard to α. In this respect, Fig. 2 presents the average mean longitudinal profile distribution along the third and last injecting block for three different α values ($\alpha = 0, -1$, and -2 deg) under similar dynamic conditions; all the data shown were obtained with a given mass flow rate and a nozzle height controlling average pressure in the chamber. The latter remained almost unaltered by the internal geometric changes due to the tapered α angle introduction. A reference velocity and corresponding Mach number were then computed by integrating the whole mass flow rate flowing through the internal chamber whose height is that of the reference case ($\alpha = 0$ deg). Without any tapered angle, flow is first sheared in the wake of the obstacle; velocity profiles evolve drastically from one location to another. Because of injecting conditions, no reversed flow is observed in the rear part of the obstacle. And then, for $X > 2.22$, the shape of longitudinal profiles ceases to change significantly and essentially fits in with the Taylor characteristic profiles, which were found to follow the trigonometric shape of a wall injection flow without any geometric perturbations; this is a well-documented shape for such a flow. Then, after local but pronounced interactions in the obstacle area, the flowfield tends to "forget" these perturbations, and profiles converge toward a distribution corresponding to what is to be expected without any emerging obstacle in the injecting wall chamber. When comparing the reference case ($\alpha = 0$ deg) with the two other distributions shown ($\alpha = -1$ and -2 deg), it is clear that the greater the proximity to the obstacle location, the more similar the velocity profiles. As upstream flows are similar whatever the α studied, so are velocity profiles at the obstacle location. However, whereas profiles more or less closely correspond to the Taylor shape profile in the rear part of the chamber, distributions are somewhat different with an α tapered angle along the injecting block, and the greater the α, the less the averaged distributions are found to agree with the theoretical profile. In addition, velocity profiles underline perturbations such as inflexional trends in the close vicinity of the injecting walls. For instance, inflexion points are clearly detected at $X = 4.44$ and 5.56 for $\alpha = -1$ deg. In the $\alpha = -2$ deg case, velocity distribution is transversely elongated but perturbations are also observed in the rear part of the chamber. The well-known inviscid Rayleigh criterion states a necessary instability condition: an unstable velocity profile

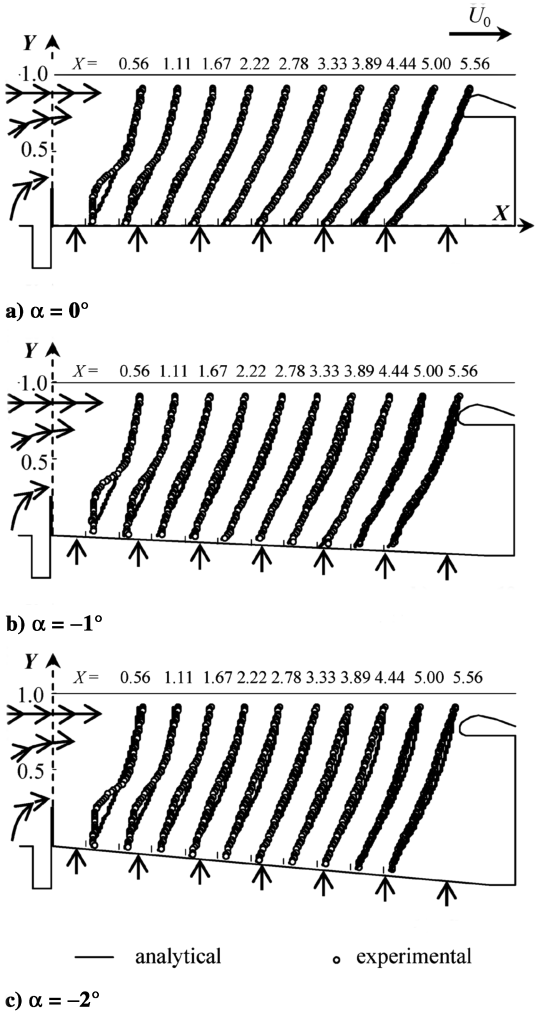

Fig. 2 Longitudinal mean velocity profiles downstream from the obstacle location vs the α porous wall inclination: experimental and analytical comparison.

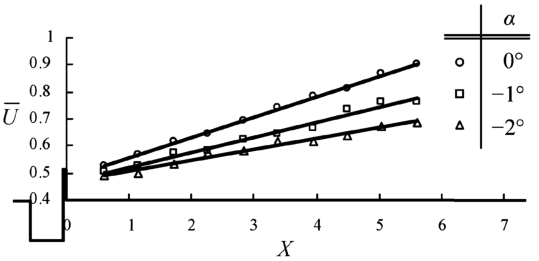

Fig. 3 Change of average velocity with regard to X and parameterized by α.

arises from an inflexion point indicating vortex development with the mixing layer. Given that the shear layer initiated in the wake of the obstacle is a strong vortex-shedding source, the introduction of an α tapered angle modifies interactions between the main flow and the one arising from the injecting walls. To shed light on main flowfield acceleration in the chamber, an average velocity $\bar{U}$ was computed from the velocity profiles shown in Fig. 2 and its modification is plotted in Fig. 3 for three angles. Our findings may be summarized as follows.

First, an overall linear trend is detected in the change of $\bar{U}$ with X, whatever be α, thereby underscoring the fact that injection of fluid all along the chamber remains constant and homogeneous. Note that this linear trend is only a first approximation because, according to its estimation, the average mean velocity slope coefficient likewise varies with X. Second, and as expected, flowfield acceleration with X

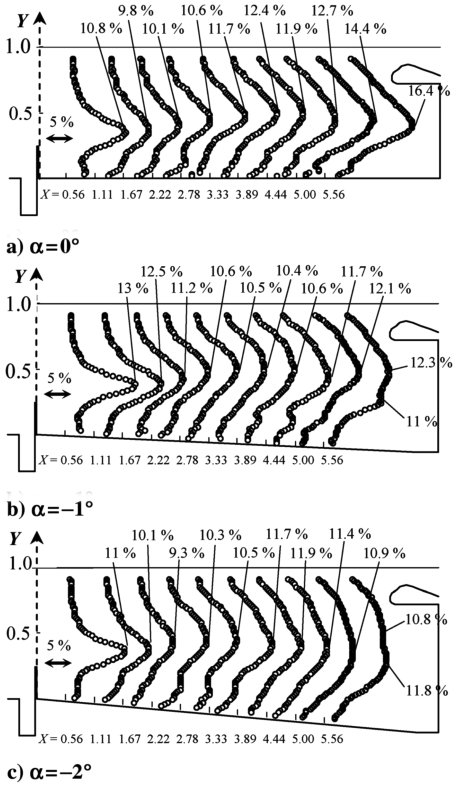

Fig. 4 Turbulent intensity *It* profiles downstream from the obstacle location vs the α porous wall inclination.

is a direct function of α, and the greater the α, the smaller the $\bar{U}$ slope. As could likewise be expected, the reduction of flowfield acceleration is due to a steady increase of the channel height with X, the increase being less pronounced with a greater α angle.

The drastic changes in velocity amplitudes naturally occasion several questions. In the first place, does such momentum balance play a key role in the unstable potentiality of the flowfield? One may also wonder whether or not these three cases are characterized by a similar reference velocity. However, let us first analyze possible changes in the fluctuating activity with regard to α.

Figure 4 shows several turbulent intensity It profiles obtained at $M = 0.09$ for three different α angle sidewalls ($\alpha = 0$, -1, and -2 deg). Whatever the internal geometry considered, the shear layer is largely dominated by strong fluctuating activity back to the obstacle ($X = 0.56$); a main peak of turbulent intensity It may be observed. The lateral location of the maximum does not depend on α and is found slightly above the top of the obstacle height. Given the way the flow contracts when passing over the obstacle, the shear layer initially develops above the obstacle height, as does its turbulent activity. And yet, whereas upstream and its average distribution are not linked to α, amplitude and It characteristic profile shapes happen to be strongly dependent on α. A possible explanation is as follows.

First, even though no unequivocal trends clearly emerge, the levels are undeniably modulated by internal geometry. Downstream from the obstacle ($X = 0.56$), maximum peaks reach 10.8, 13, and 11% for $\alpha = 0$, -1, and -2 deg, respectively, whereas, in the rear part of the chamber, the last profile shown close to the nozzle location exhibits maximum It levels equal to 16.4, 12.3, and 11.8%. Amplification of fluctuating activity is observably strongly altered with α. Second, and perhaps most important, the characteristic profile shape of turbulent intensity evolves differently with α. In the reference case ($\alpha = 0$ deg), the It peak at the shear-layer origin initially decreases while the peak spatially enlarges. However, while turbulent intensity develops transversely, its maximum level is also slightly amplified from $X \approx 2.22$. In the vicinity of the injecting walls, local turbulent intensity develops all along the chamber as though a secondary mechanism were being activated and producing fluctuating activity as well. According to several works devoted to similar geometries [14], such perturbations and production close to the injecting walls render evident the presence of another vortex-shedding mechanism. As is emphatically stated by Majdalani [24], vorticity generated along injecting walls is due to axial pressure gradient and interactions between mean flow and secondary flow originating in the porous walls. In a bidimensional cold flow analysis [14], the presence of vortices was unmistakably identified through comparison of fluorescence results with numerical computations, and wall vortex shedding was found to act as a major unstable source in SRM. In Fig. 4, it appears patent that It fluctuating activity for $\alpha = -1$ deg is stronger than that observed for $\alpha = 0$ deg at the obstacle location and that, along the chamber, It decreases slightly. Considering the fact that channel height increases continuously with X, flow stresses are in all likelihood smoother for $\alpha = -1$ and -2 deg, which may help to alter It behavior; in the rear part of the chamber, fluctuating activity is strengthened. In the $\alpha = -1$ deg case, perturbations close to the injecting walls are distinctly visible all along the chamber. For $\alpha = -2$ deg, however, these perturbations are not quite as easily detectable in the rear part of the chamber. Everything occurs as if the vortex shedding for a small α angle initiated in the obstacle wake was not strong enough to interact with the injecting flow, thereby decreasing fluctuating activity. As just pointed out, introduction of a tapered sidewall indubitably modifies spatial distribution as well as the amplitude involved; this may be explained by the fact that the α angle could have a direct impact on the balance of the two vortex-shedding mechanisms. To determine whether or not such interaction occurs, their development needs to be preliminarily observed at close range. On this subject, spectral analysis of velocity signals and head-end pressure fluctuations is summarized in Fig. 5. Two velocity probes were used to record characteristic velocity history in the obstacle wake and in the vicinity of the injecting wall in the rear part of the chamber. Spectral changes were studied for three α angles, and more than 120 different Mach number levels were used to obtain the pressure and velocity spectral contours displayed.

As we observe the spectral energy contained in signals for pressure fluctuation, at least two main trends appear connected with the M increase. First, for $M \leq 0.08$, spectral distribution is mainly driven by a single peak, which evolves with M around $f_{1L} \sim 270$ Hz. It would seem obvious that the most excited frequency evolves linearly with M and that as soon as the frequency value diverges excessively from f_{1L}, a jump in frequency occurs. Such a trend is in any event signally characteristic of an aeroacoustic coupling. However, this type of coupling is not particularly strong and, as can be observed either through the spectral velocity analysis performed in the shear layer or in the vicinity of the injecting walls, it may be characterized as weak on account of the low energy levels involved in the pressure and velocity signals. Second, a linear frequency increase is also clearly observed in the whole Mach number range studied and, within this framework, the energy involved in such transfers is considerably stronger; no jump occurs, and such evolution is likewise clearly detected in spectral analysis of the velocity component recorded, either in the shear layer or close to the injecting walls. This peak corresponds to wall vortex shedding, which had previously been detected for the low Mach number studied ($M \sim 0.06$). As the main peak was similarly detected in the signals recorded in the rear part of the chamber close to the injecting wall, rather than in the pressure answer, our findings would appear to indicate that wall vortex shedding could be a major source of instability. From a quantitative standpoint, our analysis of correlation between pressure and velocity in the shear layer and close to the injecting wall will be presented next. However, it should first be emphasized that this mechanism is dynamically driven, i.e., the frequencies involved are far below f_{1L}. As M increases, the dominant frequency augments correspondingly and, as soon as the latter narrows f_{1L}, a resonant mechanism arises, thereby explaining the large energy transfer involved. For $M = 0.08$, the natural frequency is close to f_{1L} and the energy involved in the velocity signal reaches its highest level. As a consequence, pressure waves strengthen development which helps to establish and highlight shear-layer vortex shedding.

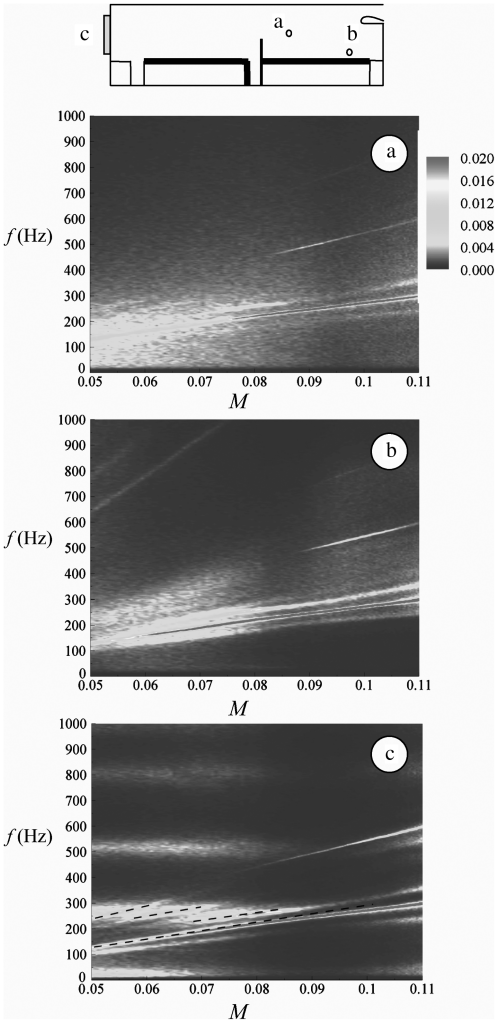

Fig. 5 Spectral analysis of a) shear layer fluctuating velocity, b) wall-injection fluctuating velocity, and c) head-end fluctuating pressure with regard to M for reference case ($\alpha = 0$ deg).

B. Identification of Aeroacoustic Coupling

From the previous analysis, the presence of strong interactions between pressure waves and wall and shear-layer vortex-shedding mechanisms has been clearly identified, even if it remains difficult to quantitatively determine which phenomenon triggers the others. To enhance description of these phenomena, we introduced correlation coefficient analysis between pressure and velocity signals. $R_{u'p'}(\tau)$ allows one to identify potential interactions between the two fields and is by far the most important point; given the τ level at which interactions take place, it may be possible to state which mechanism triggers the other one. To illustrate our hypothesis, let us just take the $R_{u'p'}(\tau)$ example in Fig. 6a. In the latter, velocity fluctuations recorded in the shear layer were correlated with pressure fluctuations at the head end for two different Mach numbers. For $M = 0.051$, $R_{u'p'}(\tau)$ is mainly characterized by two main peaks of 7.3 and 9.4%, respectively, for a negative and a positive time delay. These two main peaks in the $R_{u'p'}(\tau)$ distribution demonstrate existence of coupling between dynamics and acoustics. In accordance with sensor location and $R_{u'p'}(\tau)$ definition, correlation at a positive time delay corresponds to the fact that a velocity sensor first detects a vortex convection; the latter is convected up to the submerged nozzle and impinges upon the nozzle-generating pressure wave traveling back toward the head end. Then, τ^+ corresponds to the time convection of the vortex to the nozzle and the time taken by the pressure wave to travel back up to the head end. When the acoustic wave in its displacement back toward the head end is close to the obstacle location, it may trigger the shear layer and initiate development of another vortex. Because acoustic convection speed is much higher than flow convection, information that a new vortex has been generated is initially received by the pressure sensor at the head end, which explains why correlation at τ^- occurs. An analytical model to estimate τ^- and $\tau^+$was proposed by Vetel et al. [10], and analytical results were found to be in close congruence with the experimental data. Even if no specific analyses were conducted on the levels of $R_{u'p'}(\tau)$ reached, it is obvious that correlation levels increase when strong coupling occurs. For $M = 0.08$, the two main τ^- and τ^+ peaks reach levels equal to 25.5 and 25%, respectively; due to high coupling for $M \geq 0.08$, correlations also occur for higher time delays and are strongly triggered by a single frequency, i.e., $f = 220$ Hz, which was found to be the dominant one for $M = 0.08$ in Fig. 5. Moreover, it appears worth emphasizing that for $M = 0.051$, τ^- and τ^+ peaks were not triggered by any single frequency and that, in accordance with the strong variations of $R_{u'p'}(\tau)$ with τ close to τ^- and τ^+, frequencies of 270 and 130 Hz may be exhibited, respectively. The existence of these two frequencies clearly demonstrated the presence of dual behavior in the shear-layer destabilization process. Although acoustic pressure waves traveling back to the head end attempt to trigger destabilization of the shear layer at its own frequency (i.e., $f \sim 270$ Hz for τ^-), dynamic conditions at the obstacle location present unstable behavior differing from that exhibited under acoustic conditions. As regards the velocity—pressure relationship, it is important to recall the potential links with the wall vortex-shedding source. Figure 6b shows $R_{u'p'}(\tau)$ between the velocity signal recorded in the rear back of the chamber close to the injecting wall and head end pressure fluctuations. For $M = 0.051$, one main peak dominates $R_{u'p'}(\tau)$ reaching a level of 12% at τ^+. In reality, the time delay at which a 12% correlation occurs is more likely to be close to $\tau^+ \sim 0$, simply because the velocity probe is located close to the submerged nozzle location; convection time is then consecutively shorter. Thus, vorticity concentration in this area helps pressure wave generation when wall vortex shedding impinges upon the nozzle. The wide Mach number coupling range (i.e., $M = 0.08$ shown in Fig. 6b) underscores the exceedingly high correlation levels for either positive or negative time delay. A resonant phenomenon occurs, i.e., the two vortex-shedding mechanisms align with each other.

As already pointed out in the fluctuating flowfield analysis, introduction of an α inclination angle may modify interactions between the two vortex-shedding sources and coupling phenomena, as well.

IV. Impact of α on Coupling

So as to bring into relief unstable development pertaining to α, spectral analysis of the head-end pressure fluctuations was carried out with regard to M level for several α angles. To emphasize spectral analysis change, Fig. 7 shows spectral analysis obtained for $\alpha = -1$ and -2 deg, and the developments recorded should be compared with the evolution observed for the reference case ($\alpha = 0$ deg) in Fig. 5. Attempting such comparison is highly interesting insofar as it brings several specific trends into close focus. First and foremost, duality mechanisms enter into play whatever α is studied, i.e., in the low Mach number range ($M \leq 0.08$), a weak coupling occurs, whereas up to a threshold Mach number, energy concentrates around a single frequency, which increases linearly with M. Second, the lower the α, the higher the threshold Mach number. In fact, everything takes place as though introduction of α angle inclination were only serving to delay vortex-shedding mechanism interaction. To check such an assumption, it is initially necessary to analyze the frequency involved in the coupling area with regard to α. Figure 7 presents the plot of the most excited frequency with M, whatever be α; in the $M \geq 0.08$ range, and it appears obvious that linear increases are similar but decayed in M. Moreover, one may fairly conclude that no clear trend is detected with regard to α. One ought nevertheless to bear in mind that introduction of an α angle modifies mean flowfield behavior and that the lower the α, the lower the flowfield acceleration. The characteristic Mach number should then be adapted to the geometry configuration, i.e., linked to α. To take increased chamber height into account, we introduced a modified M^*

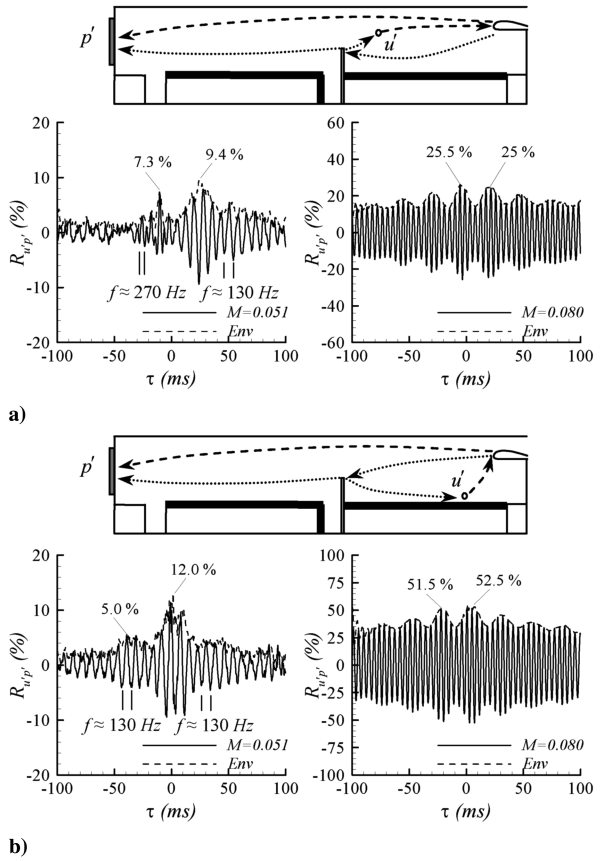

Fig. 6 Cross-correlation coefficient between pressure fluctuations and a) shear-layer velocity fluctuations and b) wall velocity fluctuations.

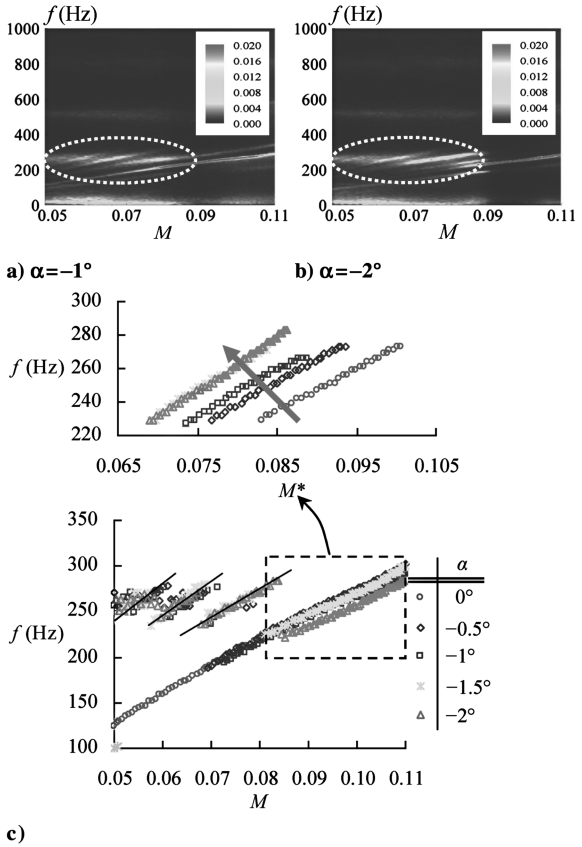

Fig. 7 Spectral analysis of head-end fluctuating pressure with regard to M for a) $\alpha = -1$ deg, b) $\alpha = -2$ deg, and c) main frequencies of head-end pressure spectra vs M with regard to α.

Mach number; Fig. 7 indicates the highest excited frequencies with regard to M^*. Two main points may be stressed: First, for $-1 < \alpha < 0$ deg, stratification is accentuated, i.e., the linear increase commences for smaller M^* with the decrease of α. Thus, the preceding assumption appears correct and a shift in the mechanism is introduced with α. However, such a shift in M^* is not observed for $\alpha < -1$ deg and the results obtained for $\alpha = -1.5$ and -2 deg are similar. To conclude, it seems obvious that two main trends are being exhibited, and a threshold α angle in between -1 and -1.5 deg has been identified. Although it would appear that two different trends may be rendered evident with α, it is interesting to quantify the latter in terms of energy level involved. To do so, Fig. 8 presents the change in $\sqrt{\overline{p'^2}}/P$ oscillation levels detected at the head end with regard to α for several M numbers. To pinpoint α influence on flowfield behavior, $\sqrt{\overline{p'^2}}/P$ changes with α have been shown for $M = 0.09$ and 0.10. For $M = 0.09$, the energy level involved initially decreases with α and would appear to reach a minimum level for $\alpha \sim -1.5$ deg before increasing sharply for $\alpha < -1.5$ deg. Taking as a reference the energy level to be found at $\alpha = 0$ deg, a decrease of approximately 50% is observed between $\alpha = 0$ and $\alpha = -1.5$ deg, whereas only a 30% decrease occurs between $\alpha = 0$ and $\alpha = -2$ deg. A similar trend is obtained for $M = 0.1$ where the maximum level is reached at $\alpha = -1.5$ deg and the increase phase is pronouncedly more

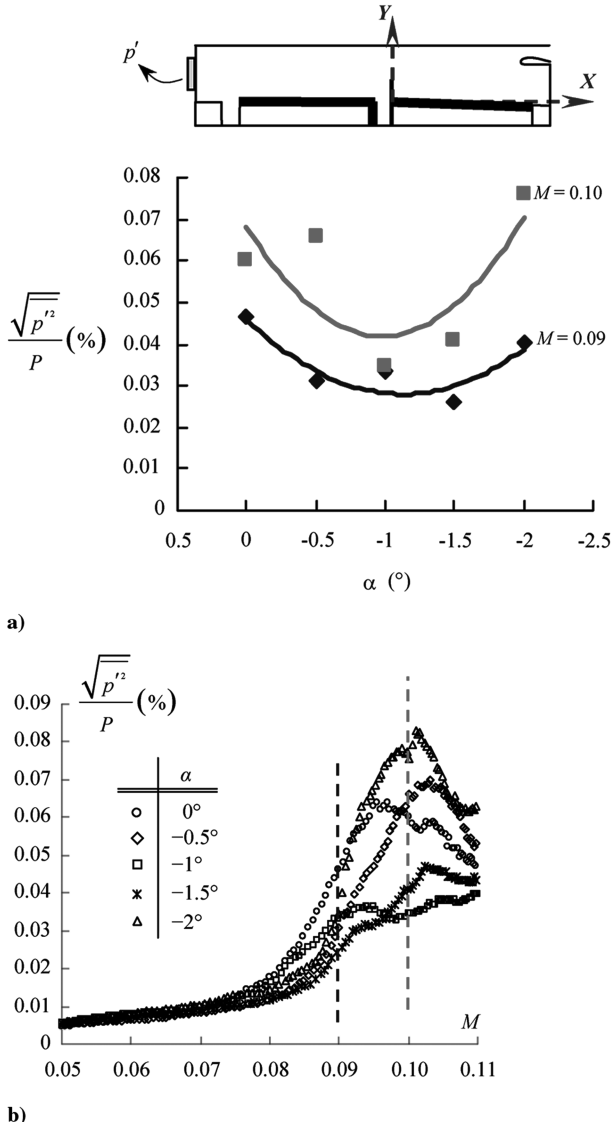

Fig. 8 Change in $\sqrt{\overline{p'^2}}/P$ oscillation levels detected at the head end with regard to α for a) $M = 0.10$ and 0.09, and b) several M numbers.

significant, with a 30% energy increase from $\alpha = 0$ to -2 deg. Note that while the α angle varies from 0.5 deg, minimum energy levels may be reached in between two α levels studied, and yet the main feature nonetheless remains depicted.

To conclude our considerations on the impact of α on flowfield behavior, two main and opposed phases have been identified with α. The first one corresponds to a reduction in energy present for the lowest angle inclination studied and, according to frequencies, seems to correspond to a linear shift in the vortex-shedding mechanisms. An amplification phase occurs as soon as a minimum energy level is reached and is detected for the lowest α level studied ($\alpha < -1$ deg). Even if these results do not explain why these two opposed phases occur, they are of substantial importance insofar as they demonstrate that the α tapered sidewall effect is a major factor as regards pressure oscillation levels in segmented chambers.

At this point in our study, we are attempting to understand why reduction and amplification phases occur. To do so, one may analyze flowfield behavior by following spatial development of the two vortex-shedding mechanisms. Because of porous wall conditions, direct identification of vortex generation (by a visualization technique, for instance) is not possible. And so, from velocity signals recorded by hot-wire probe and given the fact that a single frequency predominates in the spectral answer, a phase-average technique was applied to assess the Z vorticity vector component by applying the Taylor temporal-velocity relationship as

$$\Omega_z(x_0, y, \tau) = -\frac{\partial\langle u\rangle(x_0, y, \tau)}{\partial y} - \frac{1}{\bar{u}(x_0, y)}\frac{\partial\langle v\rangle(x_0, y, \tau)}{\partial \tau}$$

Following that, the Ω_z definition was applied to velocity signals obtained for $\alpha = 0$, -1, and -2 deg under similar dynamic conditions ($M = 0.09$), and spectral distribution is indeed found to be mainly dominated by the one frequency considered for the phase-average procedure. This technique specifically provides the change of Ω_z in time within the frequency period considered at a specified longitudinal location; Ω_z can be estimated all along the channel height by reapplying the phase-average procedure. Figure 9 shows Ω_z contours obtained for several longitudinal locations while time and vertical direction were discretized by 100 and 50 intervals, respectively. White dashed lines in Fig. 9 are added to mark the convected vorticity arising from the shear-layer instability and wall generation. At first glance, it appears evident that the phase-average procedure facilitates precise depiction of the two vortex-shedding phenomena, i.e., the shedding in the thermal inhibitor wake and the

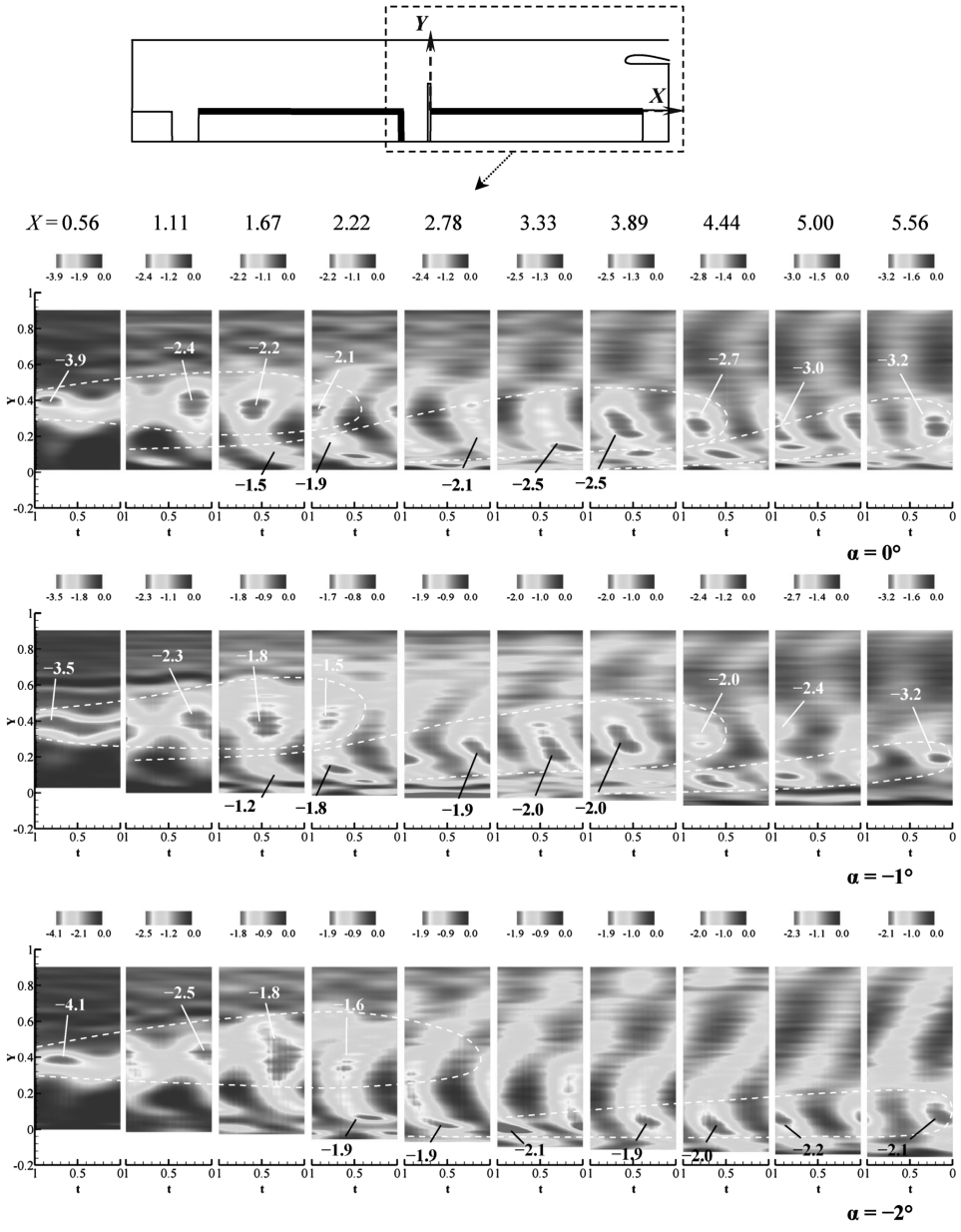

Fig. 9 Phase average of Ω_z vorticity component contours downstream from the obstacle location with regard to $\alpha = 0, -1$, and -2 deg.

shedding all along the injecting walls. Note that if vortices are not clearly detected in the rear part of the chamber and in the main flow, this is mainly due to a wider frequency spectral answer in that area. However, the Ω_z contours shown offer us a complete and accurate picture of flowfield behavior all along the chamber. Several points may be stressed. First, even with similar upstream flow conditions, amplitude of Ω_z at the inhibitor location is increased for $\alpha = -2$ deg and such a trend is in agreement with the one depicted for $\sqrt{\overline{p'^2}}/P$ change with regard to α (Fig. 8). Second, the longitudinal location at which wall vortex may be identified is similar whatever α ($1.67 \leq X \leq 2.22$), although, on the contrary, its behavior all along the chamber appears to be strongly modulated by α. For $\alpha = 0$ deg, everything occurs as though the vorticity at the wall produced by the high shear of the injected flow were directly feeding the main flow instability. Interactions between the two mechanisms arise in the vicinity of the injecting walls. For $\alpha = -1$ deg, the wall vortex structures are found to develop further away from the structures in the shear layer than in the reference case. This result may be explained by the continuous increase of chamber height, even if interactions without merging occur between the two vortex-shedding phenomena. Coherent structures are consequently larger but also weaker than those observed for $\alpha = 0$ deg, especially in the rear part of the chamber ($X \sim 5.56$ for instance). If physical distance between the two vortex-shedding mechanisms were the only key parameter, one might safely predict that at a smaller tapered sidewall angle, a pronouncedly greater decrease in structures would be observed. Quite on the contrary, given the Ω_z contours in that condition, vortex structures at the rear end are actually larger and stronger than those observed for $\alpha = -1$ deg. Because of higher pressure levels, vortex structures in the shear layer are likewise stronger and are convected within the main flow. As is graphically illustrated in Fig. 9 for $\alpha = -2$ deg, vortex structures are no longer attracted toward the injecting walls. Vortex in the main flow always triggers development of wall vortex shedding and, from that point, vorticity concentration close to the wall is kept within that area all along the chamber and no longer merges with main flow vortex emanating from the shear-layer development. As a consequence, it would seem obvious that the injecting condition directly feeds wall vortices; Ω_z levels continuously increase along the chamber and the wall structure spatially develops in a similar manner. At the same time, characteristic levels of main flow vortex are not as significant. In conclusion, α effect is a major contribution insofar as it directly modulates the distance separating the two mechanisms. To better understand these opposed effects, a space-time correlation was analyzed with regard to α.

First, $R_{u'p'}(\tau)$ correlations are plotted in Fig. 10 for $\alpha = 0, -1$, and -2 deg under the same dynamic condition ($M = 0.06$). Whereas aeroacoustic coupling is clearly detected for $\alpha = 0$ deg with the emergence of the two peaks at both positive and negative time delays, the impact of shear layer on pressure wave generation is significantly reduced with correlation level at τ^+ of 6% for $\alpha = -1$ deg, whereas for $\alpha = -2$ deg, almost no significant correlation is observed. However, pressure waves still initiate vortex shedding at the obstacle location with τ^- correlation levels of 12.5 and 7.5% for $\alpha = -1$ and -2 deg, respectively. Under these dynamic conditions, it is clear that aeroacoustic coupling is markedly weakened with α. To quantitatively detect the interaction level between the two vortex-shedding phenomena, we have computed the cross correlation $R_{u'_s u'_w}$ (Fig. 11), in which s and w subscripts designate fluctuations recorded in the shear layer close to the obstacle location and in the vicinity of the injecting wall at the rear end of the chamber, respectively. The strong $R_{u'_s u'_w}(\tau)$ correlation at τ^+ for $\alpha = 0$ deg indicates that shear-layer development fully triggers vorticity generation at the injection wall. Moreover, the perturbations involved in shear-layer development favor vorticity concentration close to the injecting wall. Actually, even if $R_{u'_s u'_w}(\tau)$ correlation is still significant for $\alpha = -1$ deg with a peak correlation at 9%, almost no link arises between the two vortex-shedding phenomena with a tapered side angle at $\alpha = -2$ deg. The α inclination effects consist in favoring the spatial separation between vortices from the shear layer and the injecting

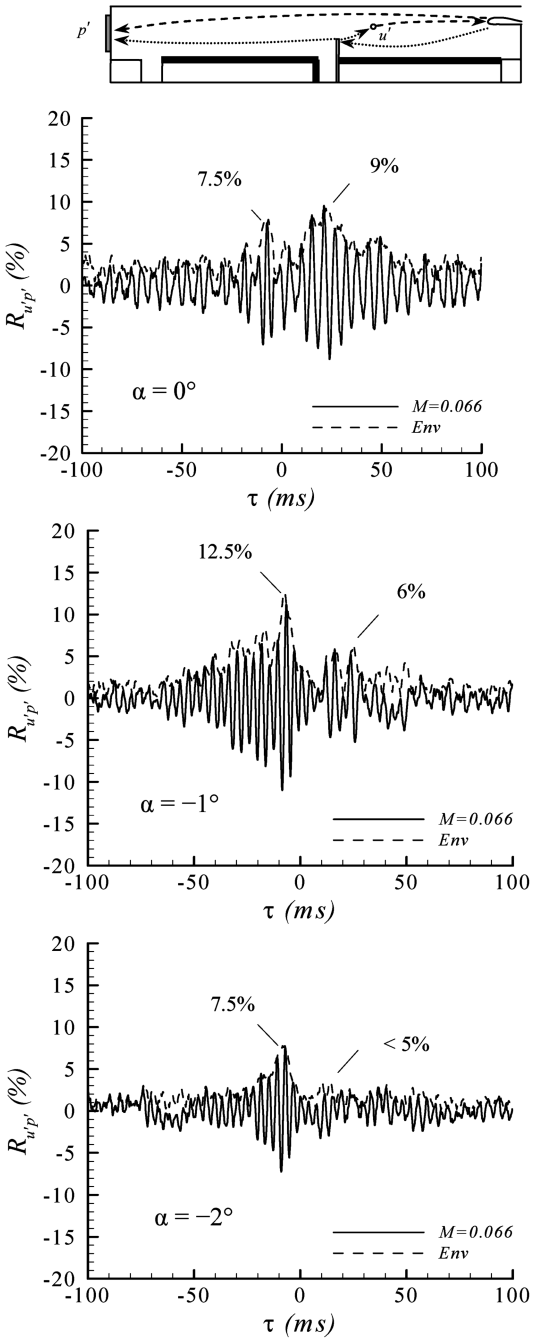

Fig. 10 Cross-correlation coefficient between pressure fluctuations and shear-layer velocity fluctuations with regard to $\alpha = 0, -1$, and -2 deg.

wall. To shed light on this separation, spectral analysis of velocity signals along the chamber might be helpful. Figure 12 allows the observer to monitor spectral density distribution along the chamber height for several longitudinal locations and angles.

Whatever the α angle considered, velocity spectral activity in the obstacle area ($X = 0.56$) is mainly characterized by a spatial peak in the obstacle wake that corresponds to the vortex shedding arising from the obstacle; amplitude levels are modulated in a way similar to pressure fluctuations, i.e., a decrease in the energy involved is observed from $\alpha = 0$ to -1 deg, whereas levels increase from -1 to -2 deg. In the reference case ($\alpha = 0$ deg), levels are strongly amplified along the chamber; for $X = 2.22$, a second spatial vorticity development is detected, and it corresponds to the development of the wall vortex-shedding mechanism. To better understand spectral change along the chamber, it appears useful to analyze the development of spectral activity in conjunction with the spatial

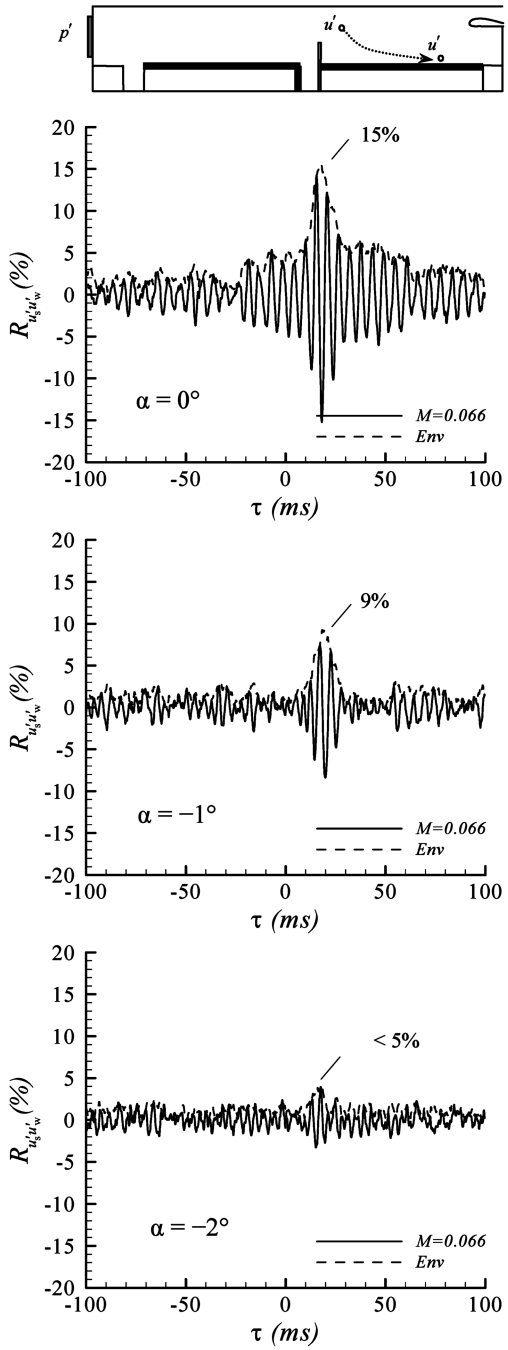

Fig. 11 Cross-correlation coefficient between shear-layer velocity fluctuations and wall injection fluctuations with regard to $\alpha = 0, -1$, and -2 deg.

vorticity shown in Fig. 9. From $X = 0.56$ and 2.22 (i.e., locations 1 and 2), wall vorticity literally merges into the main flow structures, thereby explaining the significant increase of the spectral peak in the main flow. As soon as merging between the vortices occurs, wall vortex concentration once again occurs, along with the emergence in the spectral activity of a new peak. In the rear part of the chamber, i.e., between locations 3 and 4, similar behavior takes place, i.e., wall vortex structure develops and merges into main vortex structures. As a consequence, a single peak distributing along the whole channel height comes into being, and its level is strongly amplified. For $\alpha = -1$ deg, similar trends may be observed for positions 1, 2, and 3, but the energy levels detected are significantly smaller than those involved in the reference case. As clearly observed in the spatial evolution of the Z vorticity component (Fig. 9), main wall injection structures interact with each other, thereby significantly weakening their coherence, even if levels are also amplified in the rear part of the chamber. In position 4, i.e., for $X = 5.56$, not just one but two peaks of spectral distribution of the fluctuating activity are to be observed; these two peaks naturally correspond to the main flow and to injecting wall instability, and their evident presence underscores the fact that merging is no longer arising. Quite on the contrary, it seems that the physical separation imposed by α contributes not to merging but to interaction, and that energy is lost in the process. Moreover, the way vortices organize in the rear part plays a key role because its impinging is what controls pressure wave generation. A strong correlation exists between the coherence of vortex impinging upon the nozzle and pressure wave generation. For $\alpha = -2$ deg, the distance between the two vortex-shedding sources is naturally greater than for $\alpha = -1$ deg, which contributes to significant interaction. As may be observed in the spatial distribution of fluctuations, the peak that corresponds to wall vortex shedding is totally separated from that of main flow vortex shedding. This trend is even more clearly observed in Fig. 9. In fact, the distance between the two vortex-shedding mechanisms is sizable enough to ensure interactions between structures. As a consequence, in the rear part of the chamber, the structures arising from the injecting walls are not altered during their convection along the injecting walls and, moreover, as clearly illustrated in Fig. 9, wall vortices remain in the vicinity of the injecting walls all along their convection in the chamber, thereby enhancing their coherence. When flow organizes to exit through the nozzle, strong and coherent structures arising from the injecting walls are detected at $X = 5.56$ at location 4, and they then help to significantly amplify pressure levels and coupling mechanisms.

V. Conclusions

Effects of α injecting sidewall on the internal flowfield have been investigated in the present paper and, more specifically, their influence on the vortex-shedding phenomena that occur in segmented flows. The results achieved arise from experiments conducted in a small-scale cold gas setup of an SRM. Only the third and the last injecting block were equipped with an α tapered sidewall ranging from the reference case $\alpha = 0$ to -2 deg. A detailed analysis of the reference case yields straightforward depiction of two forms of behavior with regard to the internal characteristic Mach number. In the lower Mach number range ($M \leq 0.08$), a dual phenomenon arises in the shear layer, i.e., the latter is driven by two different frequencies. The first evolves close to the first acoustic mode and exhibits a weak coupling between acoustics and flowfield dynamics, whereas the shear layer organizes following a natural dynamic frequency. For $M > 0.08$, perturbations in the main flow trigger wall vorticity development, which evolves along the injecting walls. From phase-average analysis, wall vorticity is found to feed the main vortex flow as well as the one arising from the injecting walls. The role of an α tapered sidewall is essential in the relationship, to interactions between the two vortex-shedding phenomena, and consequently in aeroacoustic coupling. Two opposite trends have been observed with regard to α. From a small inclination angle, the two vortex-shedding phenomena interact with each other in such a way that direct merging no longer arises, and yet the continuous distance between the two vortices weakens their interaction. As a consequence, vortices arising from the shear-layer development are pronouncedly lessened, as is wall vorticity. In the impinging impact region, the decrease of vorticity concentration also weakens pressure wave intensity and, as an overall result, the whole interaction chain is found to be dampened. On the contrary, for larger angles, a separation of the wall and the shear-layer vortex-shedding phenomena is observed, i.e., in this case no direct interactions are exhibited between the two mechanisms. And under that condition, the wall vortex shedding that develops along the injecting wall literally leans up against it and is strongly enhanced. Vorticity involved in the shear layer does not strongly increase all along the chamber because of a lack of "feeding" by the injecting wall condition. Such a phenomenon enhances the influence of wall vortex shedding impinging upon the rear end of the chamber, which is markedly involved in the increase of pressure fluctuation levels and

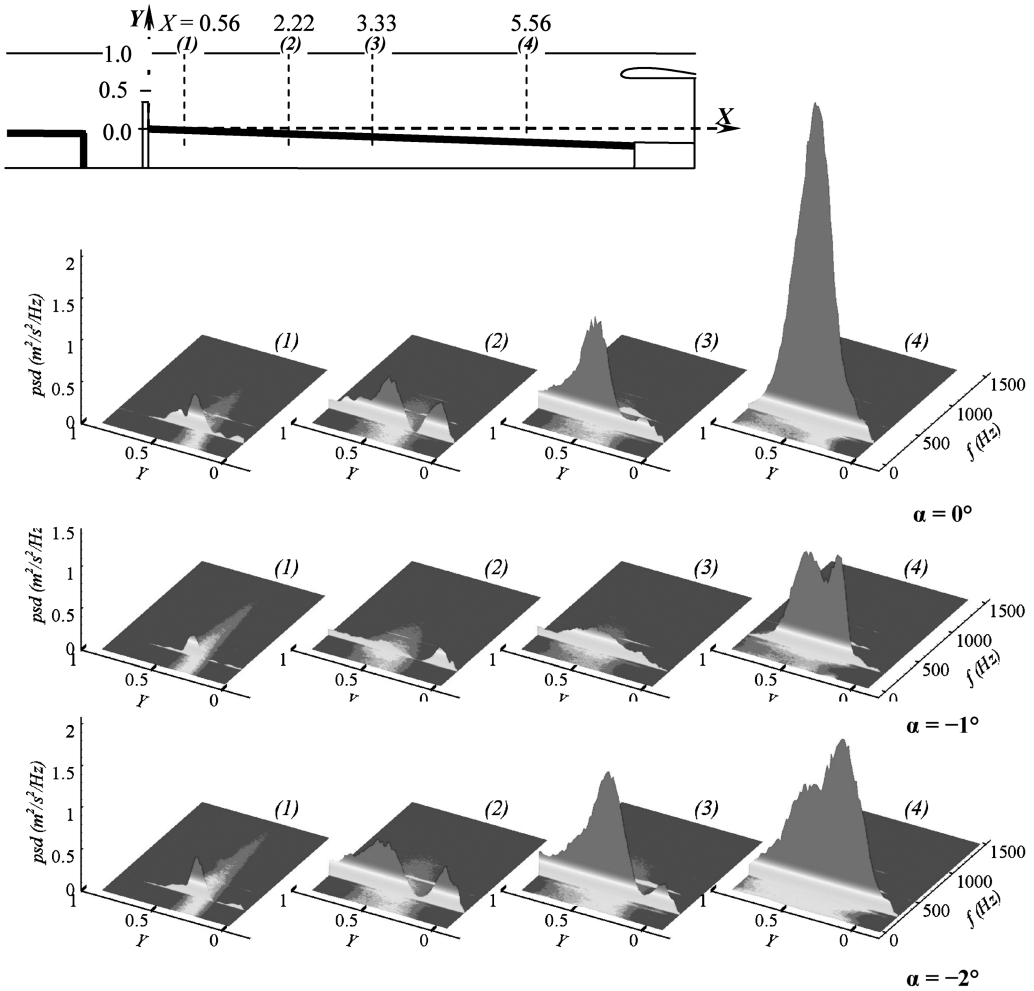

Fig. 12 Power spectral density profiles with regard to Y for several X locations ($X = 0.56$, 2.22, 3.33, and 5.56) with regard to $\alpha = 0, -1$, and -2 deg.

the strong coupling observed. The main findings of our study indeed point to the existence of a strong reduction of its coupling along with the introduction of α inclination angle. A threshold level of $\alpha = -1.5$ was clearly observed.

The present analysis constitutes one of the first steps, but not the last, as regards analysis of the α angle inclination impact on the instability that arises in SRM. It would be of prime importance to confirm these results either numerically or experimentally from firing tests conducted in small-scale SRM under optimal firing conditions. As regards cold gas setup in particular, it is clear that these setups may be useful in depiction of a possible flapper effect which may be likely to occur in the fluid/structure process of the thermal inhibitor.

References

[1] Culick, F. E. C., "Stability of One-Dimensional Motions in a Rocket Motor," *Combustion Science and Technology*, Vol. 7, No. 4, 1973, pp. 165–175. doi:10.1080/00102207308952355

[2] Vuillot, F., "Vortex Shedding Phenomena in Solid Rocket Motors," *Journal of Propulsion and Power*, Vol. 11, No. 4, 1995, pp. 626–639.

[3] Flandro, G. A., "Solid Propellant Acoustic Admittance Corrections," *Journal of Sound and Vibration*, Vol. 36, No. 3, 1974, pp. 297–312. doi:10.1016/S0022-460X(74)80212-9

[4] Flandro, G. A., and Majdalani, J., "Aeroacoustic Instability in Rockets," *AIAA Journal*, Vol. 41, No. 31, 2003, pp. 485–457.

[5] Lupoglazoff, N., and Vuillot, F., "Numerical Simulations of Parietal Vortex-Shedding Phenomenon in a Cold-Gas Set-Up," AIAA Paper 1998-3220, 1998.

[6] Apte, A., and Yang, V., "Unsteady Flow Evolution in Porous Chamber with Surface Mass Injection, Part 1: Free Oscillation," *AIAA Journal*, Vol. 39, No. 8, 2001, pp. 1577–1586.

[7] Apte, A., and Yang, V., "Unsteady Flow Evolution in Porous Chamber with Surface Mass Injection, Part 2: Acoustic Excitation," *AIAA Journal*, Vol. 40, No. 2, 2002, pp. 244–253.

[8] Apte, A., and Yang, V., "Large-Eddy Simulation Study of Transition and Flow Instability in a Porous-Walled Chamber with Mass Injection," *Journal of Fluid Mechanics*, Vol. 477, March 2003, pp. 215–225. doi:10.1017/S0022112002002987

[9] Vetel, J., Plourde, F., and Doan-Kim, S., "Dynamics of an Internal Flowfield Driven by Two Hydrodynamic Instabilities," *AIAA Journal*, Vol. 41, No. 3, 2003, pp. 424–435.

[10] Vetel, J., Plourde, F., and Doan-Kim, S., "Amplification of a Shear-Layer Instability by Vorticity Generation at an Injecting Wall," *AIAA Journal*, Vol. 42, No. 1, 2004, pp. 35–46.

[11] Dunlap, R., and Brown, R. S., "Exploratory Experiments on Acoustic Oscillations Driven by Periodic Vortex Shedding," *AIAA Journal*, Vol. 19, No. 3, 1981, pp. 408–409.

[12] Brown, R. S., Dunlap, R., Young, S. W., and Waugh, R. C., "Vortex Shedding as a Source of Acoustic Energy in Segmented Solid Rocket," *Journal of Spacecraft and Rockets*, Vol. 18, No. 4, 1981, pp. 312–319.

[13] Dunlap, R., Blackner, A. M., Waugh, R. C., Brown, R. S., and Willoughby, P., "Internal Flowfield Studies in a Simulated Cylindrical Port Rocket Chamber," *Journal of Propulsion and Power*, Vol. 6, No. 6, 1990, pp. 690–704.

[14] Avalon, G., Casalis, G., and Griffond, J., "Flow Instabilities and Acoustic Resonance of Channels with Wall Injection," AIAA Paper 1998-3218, 1998.

[15] Chedevergne, F., Casalis, G., and Féraille, Th., "Biglobal Linear Stablity: Analysis of the Flow Induced by Wall Injection," *Physics of Fluids*, Vol. 18, No. 1, 2006, pp. 014103–014114. doi:10.1063/1.2160524

[16] Taylor, G. I., "Fluid Flow in Regions Bounded by Porous Surfaces," *Proceedings of the Royal Society of London, Series A: Mathematical and Physical Sciences*, Vol. 234, No. 1199, 1956, pp. 456–475.

[17] Griffond, J., and Casalis, G., "On the Nonparallel Stability of the Injection Induced Two-Dimensional Taylor Flow," *Physics of Fluids*, Vol. 13, No. 6, 2001, pp. 1635–1644.

doi:10.1063/1.1367869
[18] Casalis, G., Griffond, J., Avalon, G., Ugurtas, B., and Vuillot, F., "Instability and Resonance in a System Simulating the Solid Propellant Motors Behavior," *2nd European Conference on Launcher Technology, Space Solid Propulsion*, ESA, 2000.
[19] Zhao, Q., Staab, P. L., Kassoy, D. R., and Kirkkopru, K., "Acoustically Generated Vorticity in an Internal Flow," *Journal of Fluid Mechanics*, Vol. 413, June 2000, pp. 247–285.
doi:10.1017/S0022112000008454
[20] Hegab, H. M., and Kassoy, D. R., "Internal Flow Temperature and Vorticity Dynamics Due to Transient Mass Addition," *AIAA Journal*, Vol. 44, No. 4, 2006, pp. 812–826.
[21] Vetel, J., Plourde, F., Doan-Kim, K., and Prevost, M., "Cold Gas Simulation of the Influence of Inhibitor Shape in Combustor Combustion," *Journal of Propulsion and Power*, Vol. 21, No. 6, 2005, pp. 1098–1106.
[22] Sams, O. C., Majdalani, J., and Flandro, G. A., "Mean Flow Approximation for a Slab Rocket Motor with Tapered Sidewalls," AIAA Paper 2003-5114, 2003.
[23] Saad, T., Sams, O. C., and Majdalani, J., "Rotational Flow in Tapered Slab Rocket Motors," *Physics of Fluids*, Vol. 18, No. 10, 2006, pp. 103601–103613.
doi:10.1063/1.2354193
[24] Majdalani, J., "Vorticity Dynamics in Isobarically Closed Porous Channel, Part 1: Standard Perturbations," *Journal of Propulsion and Power*, Vol. 17, No. 2, 2001, pp. 355–362.

T. Wang
Associate Editor